



Breaking the scaling relations of oxygen evolution reaction on amorphous NiFeP nanostructures with enhanced activity for overall seawater splitting

Jiayun Liu^a, Xuan Liu^a, Hao Shi^a, Jiahuan Luo^b, Liang Wang^a, Jiashun Liang^a, Shenzhou Li^a, Li-Ming Yang^c, Tanyuan Wang^{a,*}, Yunhui Huang^a, Qing Li^{a,*}

^a State Key Laboratory of Material Processing and Die & Mould Technology, School of Materials Science and Engineering, Huazhong University of Science and Technology, Wuhan, Hubei 430074, China

^b School of Chemical and Environmental Engineering, Anyang Institute of Technology, Anyang, Henan 455000, China

^c School of Chemistry and Chemical Engineering, Huazhong University of Science and Technology, Wuhan, Hubei 430074, China

ARTICLE INFO

Keywords:

Seawater splitting
Amorphous phosphide
Oxygen evolution reaction
Hydrogen evolution reaction
Electrocatalysis

ABSTRACT

The instinct scaling relations between the adsorption energies of key intermediates during OER lead to large overpotential for water/seawater splitting. Herein, we develop a new strategy to fabricate amorphous nickel-iron phosphides (NiFeP) with controllable morphologies as high-performance catalysts for overall seawater splitting. The ligand effect of P tunes the electronic states of the oxidized NiFe sites, thus breaks the scaling relations for OER and reduce the adsorption energy gap between HO* and HOO* from 3.08 eV to 2.62 eV. The NiFeP nanostructures exhibit extraordinarily low overpotentials of 129 mV for OER and 126 mV for HER at 100 mA cm⁻² in simulated alkaline seawater, which outperform the best reported electrocatalysts. They could also be operated at 1.57 V with 100 mA cm⁻² in a two-electrode electrolyzer and work for more than 500 h. Our work may provide a universal guidance for the design of highly active seawater splitting electrocatalysts.

1. Introduction

Water electrolysis is a sustainable and clean route to produce pollution-free hydrogen fuel with high energy density [1–3], which is essential for future renewable-energy scheme [4–6]. However, the two half reactions for water electrolysis, including hydrogen evolution reaction (HER) and oxygen evolution reaction (OER), both suffer from sluggish kinetics [7–10]. In particular, OER is more challenging due to the rigid O=O double bond and the multistep proton/electron transfer processes, which greatly hampers the overall efficiency of water electrolysis [11–13]. Moreover, the universal scaling relation between the adsorption energies of HOO* and HO* on oxide surfaces according to adsorbate evolution mechanism suggests an instinct limitation for OER activity [14]. In the past few years, a various of precious-metal free electrocatalysts such as transition metal oxides [15,16], sulfides [17,18], selenides [19,20], nitrides [21,22], phosphides [23,24] have been developed to reduce the overpotentials for OER or HER and shown great promise to replace the benchmark noble metal catalysts such as IrO₂ [25], RuO₂ [26] and Pt [27]. But a fundamental understanding on breaking the scaling relations for adsorbed OER intermediates with

adsorbate evolution mechanism still needs to be revealed to reduce the high theoretical overpotential for OER. What is more, most current researches are focused on the splitting of purified freshwater with added electrolytes [28,29]. Compared to freshwater, seawater accounts for 96.5% of the total water storage of earth and is evenly distributed in geography [30]. Therefore, overall seawater splitting is a promising candidate for mass H₂ production [3,31–33]. Recently, several electrocatalysts, including S-doped Ni/FeOOH [12], NiMoN@NiFeN [34], NiFe/NiSx-Ni [35] and Mo₅N₆ [36], have been proposed to work as either OER or HER electrocatalysts to achieve the efficient splitting of seawater. However, the rational design of highly efficient bifunctional OER/HER electrocatalysts derived from non-noble metal for seawater splitting remains highly challenging due to the complexity of the electrolyte that may lead to serious side reactions such as chloride corrosion [37,38].

Transition metal phosphides (TMPs) are promising electrocatalysts for water splitting due to the slightly higher electronegativity of P compared to most of the transition metal elements. The negatively charged P in TMPs can not only promote the splitting of water molecules in to H* or OH*, but also optimize the free energy of the adsorbed

* Corresponding authors.

E-mail addresses: wangty@hust.edu.cn (T. Wang), qing.li@hust.edu.cn, liqing830529@hotmail.com (Q. Li).

<https://doi.org/10.1016/j.apcatb.2021.120862>

Received 30 August 2021; Received in revised form 14 October 2021; Accepted 25 October 2021

Available online 29 October 2021

0926-3373/© 2021 Elsevier B.V. All rights reserved.

hydrogen atom, thus optimizing the OER and HER kinetics on the TMPs [39]. Currently, most of the studied TMPs catalysts are crystalline and limited in deionized water splitting, and there are few reports on the amorphous TMPs as bifunctional seawater splitting catalysts. Compared with crystalline TMP catalysts, amorphous phosphides would be more promising for electrocatalysis due to their abundant unsaturated active sites provided by the highly disordered structure and easily tuned elemental composition [40,41]. Simultaneously, the phosphate anion obtained by the oxidation of P may impose a repulsive effect on Cl⁻ [35], thereby avoiding the corrosion of the catalysts by Cl⁻ in seawater electrolysis. The traditional synthesis of TMPs usually releases highly toxic phosphine (PH₃), which severely hinders their practical applications from the perspective of green chemistry. Therefore, it is of great significance to develop amorphous TMP catalysts with high activity and stability for overall seawater splitting by a low toxic method.

Herein, we developed a flexible and safe solvothermal method to synthesize amorphous NiFeP with different morphologies (i.e., nanowires and nanosheets) as high-performance bifunctional electrocatalysts for seawater splitting. The as-prepared NiFeP nanowires achieve the overpotentials of 100 and 129 mV for OER at 10 and 100 mA cm⁻² and the NiFeP nanosheets display overpotentials of 83 and 126 mV for HER at 10 and 100 mA cm⁻² respectively in simulated alkaline seawater. Moreover, the operating potential for OER on NiFeP nanowires is far more negative than the thermodynamic potential for the oxidation of chloride, thus the side reaction of chloride oxidation can be avoided. Density functional theory (DFT) calculations suggest that the incorporation of P on the oxidized NiFeP surface (with NiFeOOH) can break the scaling relations of the OER intermediates and reduce the high theoretical energy barrier between HO* and HOO* (from 3.08 eV to 2.62 eV), thus significantly enhances the OER kinetics. As for HER, the presence of P can optimize the adsorption/desorption energy of H* on the amorphous NiFe structure and facilitates the reaction. During overall alkaline seawater splitting tests, the NiFeP materials can operate at a low voltage of 1.57 V at a current density of 100 mA cm⁻² and demonstrate stable response for more than 500 h, which outperforms most of the reported electrocatalysts and may serve as a promising candidate for practical seawater splitting.

2. Experimental

2.1. Pretreatment of nickel-iron foam and alkaline simulate seawater

Nickel-iron foam (Kunshan-Guangxun, China, 90 wt% Ni and 10 wt % Fe, thickness 0.15 cm) was cut into pieces with 4 cm × 0.5 cm and subsequently cleaned with alcohol and deionized water for 10 min in sequence. The alkaline simulate seawater was formulated by mixing 1.0 M NaCl (Aladdin, China, 99.8%), 1.0 M KOH (Aladdin, China, 95%) and 0.01 M KHCO₃ (Aladdin, China, 99.5%) in deionized water. The natural seawater is taken from the Bohai Sea in China and used directly without further purification.

2.2. Fabrication of NiFeP catalysts

The NiFeP electrocatalysts were synthesized by a simple solvothermal method. Typically, 0.02 mol phosphorous (Aladdin, China, > 98.9% trace metals basis, powder, -100 mesh) was dispersed in 10 mL diethylene glycol (Aladdin, China, 99%) and stirred for 30 min. Subsequently, the solution was transferred into 50 mL Teflon-lined autoclave and mixed with the pretreatment nickel-iron foam, maintained at 250 °C for 6 h, later naturally cooled to room temperature. A series of NiFeP samples with different solvothermal time (3 h, 6 h, 9 h and 12 h) were composed by the same way and the catalysts were named as NiFeP-NP, NiFeP-NW, NiFeP-NS and NiFeP-TF according to their morphologies. For temperature comparison, a series of NiFeP samples with different solvothermal temperatures (150 °C, 200 °C and 250 °C) were synthesized by the same procedure for 6 h or 9 h with the addition of 0.02 mol

phosphorous and the as-prepared NiFeP materials were denoted as NiFeP-150-6 h, NiFeP-200-6 h, NiFeP-NW, NiFeP-150-9 h, NiFeP-200-9 h and NiFeP-NS. Besides, a series of NiFeP samples with different amounts of phosphorous (0.01 mol and 0.04 mol) were fabricated by the same process at 250 °C for 6 h or 9 h and the samples were named as NiFeP-250-6 h-0.01, NiFeP-250-6 h-0.04, NiFeP-250-9 h-0.01 and NiFeP-250-9 h-0.04.

2.3. Electrochemical performance of NiFeP catalysts

The as-prepared NiFeP electrocatalysts were either tested directly or characterized after being activated at a constant current density of 100 mA cm⁻² for alkaline simulate seawater splitting in a two electrode electrolyzes systems with the same NiFeP samples as the counter electrode for 24 h. The electrochemical activated NiFeP electrocatalysts were denoted as NiFeP-150-6 h-OER, NiFeP-200-6 h-OER, NiFeP-250-6 h-0.01-OER, NiFeP-250-6 h-0.04-OER, NiFeP-NP-OER, NiFeP-NW-OER, NiFeP-NS-OER, NiFeP-TS-OER for the samples activated on the anode and NiFeP-150-9 h-HER, NiFeP-200-9 h-HER, NiFeP-250-9 h-0.01-HER, NiFeP-250-9 h-0.04-HER, NiFeP-NP-HER, NiFeP-NW-HER, NiFeP-NS-HER, NiFeP-TS-HER for the samples activated on the cathode.

2.4. Fabrication of IrO₂/C and Pt/C loaded electrodes

IrO₂/C commercial catalyst or 20% Pt/C commercial catalyst was dispersed in ethanol (Aladdin, China, 99%) with 5% Nafion and ultrasonicated for 30 min. Later, the solution was loaded on the surface of nickel-iron foam with a loading of 0.1 mg cm⁻² for IrO₂ or 20% Pt/C catalysts.

2.5. Materials characterization

Scanning electron microscopy (SEM) was carried out with a Nova NanoSEM 450 (FEI, USA). Transmission electron microscopy (TEM) characterizations were obtained on a Tecnai G2 transmission electron microscope (FEI, USA). HAADF-STEM was carried out by a Tecnai F30 high resolution transmission electron microscope (FEI, USA). X-ray diffraction (XRD) patterns were obtained using a DMAX-2400X-ray diffractometer (Rigaku, Japan). Raman measurements were performed using a LabRAM HR Evolution (Horiba JobinYvon, France) with 532 nm excitation wavelength. X-ray photoelectron spectroscopy (XPS) was carried out with an Axis-Ultra DLD-600 W X-ray photoelectron spectrometer (Shimazu, Japan). X-ray fluorescence (XRF) patterns were obtained from EAGLE III operated at 40 kV.

2.6. Electrochemical characterization

The OER and HER polarization curves were carried out with a CHI 760D (Chenhua, China) electrochemical workstation in pretreatment alkaline simulate seawater with a typical three-electrode system at room temperature. The as-prepared NiFeP sample was used as the working electrode for electrochemical characterizations, the saturated calomel electrode (SCE) was used as reference electrode and a commercial carbon rod was used as counter electrode. The potential was calibrated to reversible hydrogen electrode (RHE) through measuring the potential difference between the SCE and RHE. The long-time overall water splitting stability curves were carried on a LAND C3001B battery measurement system (Wuhan, China) in the alkaline simulate seawater and the different NiFeP electrodes were used as cathode and anode, respectively. All three-electrode electrochemical measurements are compensated by 70% iR (a larger percentage of compensation will cause excessive noise in the test curve).

2.7. Computational details

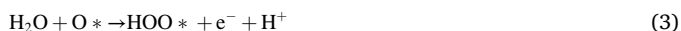
Density functional theory as implemented in the Vienna Ab-initio Simulation Package (VASP) was employed to optimize geometry structures for Fe/P doped NiOOH and Fe/P doped Ni [42,43]. The exchange-correlation interactions were described by the generalized gradient approximation (GGA) in the form of the revised Perdew-Burke-Ernzerhof functional (RPBE) [44]. A cut-off energy of 500 eV for plain-wave basis sets was adopted and the convergence threshold was 10^{-5} eV, and 5×10^{-3} eV/Å for energy and force, respectively. The weak interaction was described by DFT+D3 method using empirical correction in scheme of Grimme [45]. The vacuum space was set to be more than 20 Å, which was enough to avoid the interaction between periodical images. For Ni and Fe atoms, the Hubbard-U frameworks have been used, with 6.6 eV and 3.5 eV of Ueff values for Ni and Fe atoms, respectively.

The reaction Gibbs free energy changes (ΔG) for each elementary step were based on the computational hydrogen electrode model, which can be calculated by the following equation;

$$\Delta G = \Delta E + \Delta ZPE - T\Delta S$$

where ΔE is obtained directly from DFT calculations, ΔZPE is the change of zero-point energies (ZPE), T is the temperature of 298.15 K, and ΔS is the change in entropy of products and reactants.

The structures of OER process that P-incorporated NiFeOOH was designed by the model developed by D. Friebe et al. [46]. For the NiOOH (0 1 $\bar{1}$), a four-layer of 2×3 supercell has been applied with the last two layers fixed during the calculation. Since the substitution of Fe into γ -NiOOH could increase the OER activity, the substitution of P into γ -NiFeOOH was further modeled to see the origin of the higher activity. Different numbers of oxygen atoms on the γ -NiFeOOH surface are replaced by P atoms to construct different models, which are named NiFeOOH-P and NiFeOOH-P₂, respectively. The OER free energy profiles were derived using the standard procedures. The elementary steps, from H₂O to HO*, then O*, then HOO*, were taken to occur for OER. As correspondence, the free energies of



with * representing the metal site on the surface, were calculated. The reversible hydrogen electrode (RHE) was used as a reference to express the chemical potentials of electrons $G[\text{e}^-]$ and protons $G[\text{H}^+]$.

According to the results of XRD and XPS, the amorphous NiFe and NiFeP models were built after fully relaxing the crystal models at 1600 K and completely destroying the ordered atomic arrangement [47]. Moreover, the Ni₁₂P₅ model was built by cutting the surface of crystal Ni₁₂P₅ along the (101) directions. The vacuum space along the z direction of all the above models was set to be 15 Å. The HER free energy curve is derived using standard procedures. For HER, the basic steps from H₂O to H* and then H₂ were taken, with H* to represent the adsorbed H atoms on the surface for calculations. According to previous work, the strength of hydrogen bonds on the surface will limit the rate of hydrogen evolution reaction through the adsorption (Volmer) and desorption (Heyrovsky/Tafel) steps [48]. According to the Volmer–Tafel or the Heyrovsky mechanism, the Gibbs free energies of hydrogen adsorption (ΔG_{H^*}) is considered to be a good descriptor for catalyzing hydrogen generation [49]. In general, the closer the $|\Delta G_{\text{H}^*}|$ to zero, the higher is the activity of the sites [50]. Thus, reducing $|\Delta G_{\text{H}^*}|$ of the amorphous NiFe structure will facilitate the adsorption and desorption of H atoms. Therefore, the adsorption energy of transition metals for H* can be reduced by doping with non-metal atoms (such as phosphorus atoms, etc.). The calculated potential is relative to reversible hydrogen

electrode (RHE).

3. Results and discussion

3.1. Synthesis and characterization

The synthesis of amorphous NiFeP has been depicted in Fig. 1a. The NiFeP nanostructures were synthesized by reacting nickel-iron foam (NIF, Ni: Fe = 9: 1) with red phosphorus in diethylene glycol (DEG) at 150–250 °C. The concentration of phosphorus monomer is suggested to control the directional growth of the material on the surface of the nickel-iron foam [51,52]. In addition, DEG as an organic medium may coordinate with the metal sites and benefit the self-assembling of the materials at the atomic level [52,53]. Hence, by controlling the reaction time, temperature and the amount of added red phosphorus, the morphology of NiFeP can be adjusted to nanoparticles, nanowires, nanosheets and thick flakes, respectively. As shown in the scanning electron microscopic (SEM) images (Fig. S1, Supporting Information), the morphologies of NiFeP materials exhibit a change from nanoparticles to nanowires, nanosheets and thick flakes with the increase of the reaction time from 3 h, 6 h, 9 h, to 12 h at 250 °C with 0.02 mol red phosphorus precursor and these samples are named as NiFeP-NP (nanoparticles), NiFeP-NW (nanowires), NiFeP-NS (nanosheets) and NiFeP-TF (thick flakes) according to their morphology, respectively. As the reaction temperature increases from 150 °C, 200 °C and 250 °C, the proportion of nanowires or nanosheets on the surface of NiFeP materials gradually increases (Fig. S2, Supporting Information). Simultaneously, the surface morphology of the materials changes from nanowires or nanosheets to large particles by adding more phosphorus (Fig. S3, Supporting Information). Specifically, NiFeP-NW and NiFeP-NS show unique “electronic wire” morphology with interwoven nanowires in the diameter of 150–200 nm and nanosheets respectively (Fig. 1b, c), which may benefit charge transfer during electrochemical reactions. The elemental compositions of NiFeP samples were characterized by X-ray fluorescence (XRF). The phosphorus contents in NiFeP-NP, NiFeP-NW, NiFeP-NS and NiFeP-TF are 14.92%, 21.81%, 28.43% and 36.26%, respectively (Tables S1, S2, Supporting Information).

X-ray diffraction (XRD) is used to illustrate the crystal structures of the synthesized NiFeP. The diffraction peaks of NiFeP-NP, NiFeP-NW and NiFeP-NS are mainly the basal peaks of nickel-iron foam, which are consistent with the (111), (200) and (220) planes of cubic phase Ni (PDF# 04–0850) (Fig. 1d). No diffraction peak of crystalline phosphide is observed. However, when the reaction time reaches 12 h, the NiFeP-TF sample shows a typical crystal structure of cubic Ni₁₂P₅ (PDF# 22–1190), indicating that the amorphous NiFeP materials will transform into a crystalline Ni₁₂P₅ structure as the reaction time increases (Fig. S4, Supporting Information). The amorphous feature of NiFeP makes it a promising electrocatalyst for highly efficient water splitting since amorphous phosphides may show metallic behaviors and high concentrations of unsaturated sites, thus can increase the conductivity and the numbers of active sites for the catalysts [40]. In addition, part of the oxidized phosphorus element in the NiFeP electrodes may demonstrate a repelling effect on Cl[−] in seawater during OER [35].

Previous work reveals that transition metal compounds usually undergo irreversible surface reconstructions after OER and HER processes, which would affect their catalytic performance [54]. For example, the in-situ formed oxides/(oxy)hydroxides on the surface of many transition metal compounds during OER are suggested to be the main active species for OER [55,56]. TMPs would also be subject to surface reconstruction during electrocatalytic water splitting, resulting in enhanced activity [24]. Therefore, the as-synthesized NiFeP samples are first preactivated at a constant current density of 100 mA cm^{−2} under OER (anodic current) or HER (cathodic current) conditions for 24 h before the evaluations of their electrocatalytic performance. After electrochemical activations, NiFeP samples basically maintain their original amorphous structures (Figs. 1d and S5–S7, Supporting Information). The

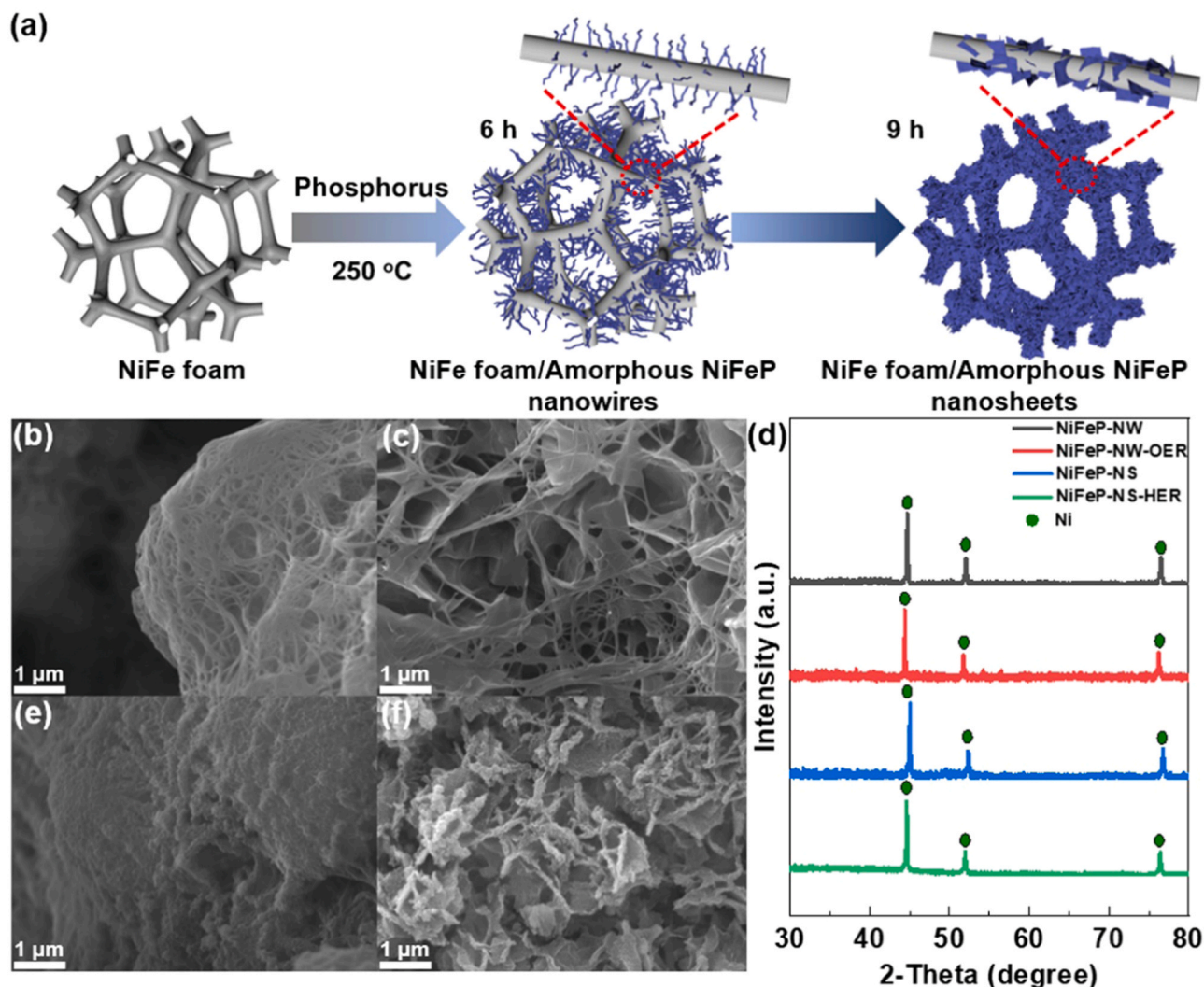


Fig. 1. Preparation and structural characterizations of NiFeP. (a) Schematic synthetic procedure for NiFeP. (b, c) SEM images of NiFeP-NW and NiFeP-NS. (d) XRD patterns of NiFeP. (e, f) SEM images of NiFeP-NW-OER and NiFeP-NS-HER.

extremely weak diffraction peaks for NiFeP-NW-OER materials at 54° and 56° may correspond to the (121) and (220) crystal planes of γ -FeOOH (JCPDF No. 70-0713), respectively, indicating that low-crystalline NiFe (hydroxy) hydroxide may be formed on the surface of NiFeP materials after OER activation. SEM images further confirm the relative stability of the NiFeP (Figs. 1e, f and S8–S10, Supporting Information). After OER or HER activation, NiFeP-NW-OER (NiFeP-NW electrodes after 24 h OER test) and NiFeP-NS-HER (NiFeP-NS electrodes after 24 h HER process) almost keep the interwoven nanowires and nanosheets morphologies except for the existence of some small particles on the surface. One possible explanation is that the OER process may be accompanied by surface oxidation, thus the surface of the materials is reconstructed and becomes fluffier, while NiFeP-NS may also perform weak surface reconstruction during HER. The transmission electron microscopic (TEM) images of NiFeP-NW and NiFeP-NS before and after electrochemical activation are shown in Fig. S11 (Supporting Information) and Fig. 2. TEM images also prove the fluffier nanowire structure of NiFeP-NW-OER (Fig. 2a). Moreover, a few weak lattice fringes can be observed on the surface of amorphous NiFeP-NW after OER activation according to the high resolution TEM image of NiFeP-NW-OER (Fig. 2b), further certifying the surface reconstruction of NiFeP-NW during OER test. The interplanar distance of the lattice fringes is estimated to be 0.16 nm, which is close to interplanar distance of (110) planes for γ -FeOOH (JCPDF No. 70-0713), indicating the possible formation of low

crystalline NiFe (oxy)hydroxides with a thickness of several nanometers (the region between the red dashed line and the blue dashed line in Fig. 2b) on the surface of NiFeP-NW after OER activation. On the other hand, the NiFeP-NS almost maintains its original structure after HER activation (Fig. 2d, e), suggesting a weaker surface change. The trace amount of lattice fringes with interplanar distance of 0.16 nm in the boundary (red dashed line in Fig. 2e) of amorphous NiFeP nanosheets and the carbon film may originate from the surface oxidation of NiFeP-HER during TEM sample preparation. The fast Fourier transform (FFT) images for NiFeP-NW, NiFeP-NS, NiFeP-NW-OER and NiFeP-NS-HER (insets of Figs. 2a, b and S11a, b, Supporting Information) all display a diffuse center spot, indicating the maintain of amorphous structure for these samples, which are consistent with their XRD patterns. Elemental mappings of NiFeP-NW-OER and NiFeP-NS-HER further confirm the presences and uniform distributions of Ni, Fe and P on the samples after electrochemical activations (Fig. 2c, f).

3.2. Catalytic performance of NiFeP for OER, HER, and overall seawater splitting

The OER and HER activity of the NiFeP materials were measured in alkaline simulate seawater at a scan rate of 10 mV s⁻¹ in a typical three-electrode system. Fig. 3a displays the OER polarization curves of NiFeP-NW, NiFe-foam (before and after OER activation), and NiFe-foam load

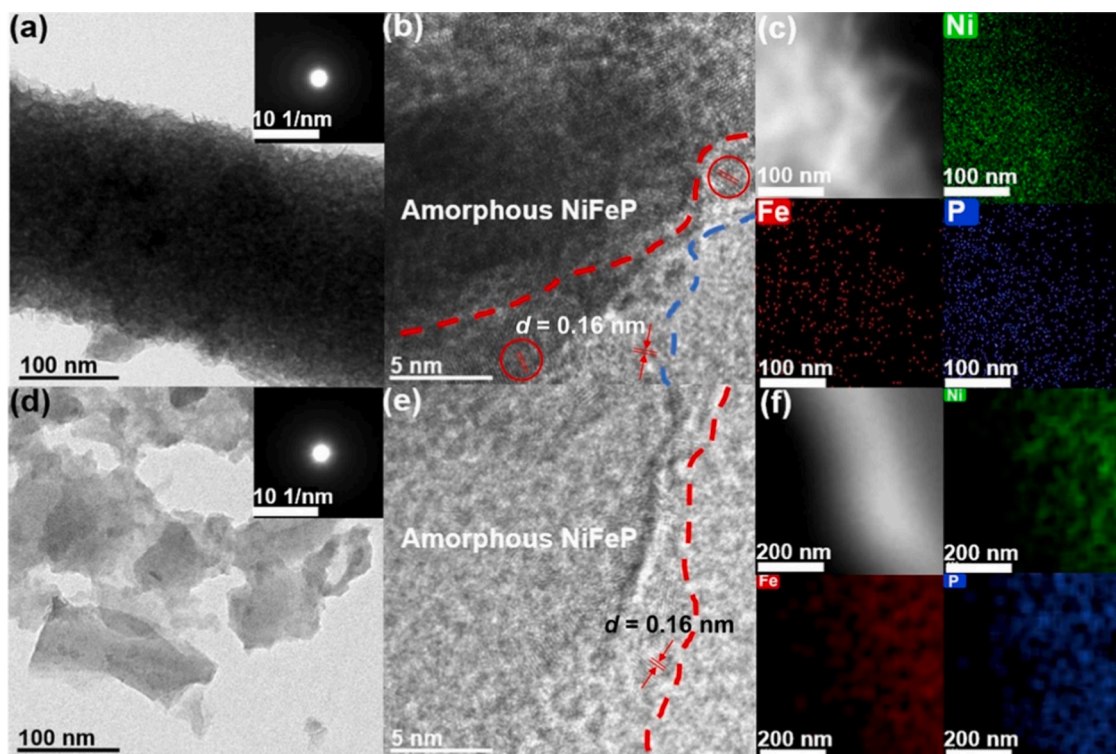


Fig. 2. Structural characterizations and elemental mappings of NiFeP. TEM images and (inset) corresponding FFT images of (a, b) NiFeP-NW-OER and (d, e) NiFeP-NS-HER. High-angle annular dark field scanning transmission electron microscopic (HAADF-STEM) images of (c) NiFeP-NW-OER, (f) NiFeP-NS-HER and the corresponding elemental mappings of Ni, Fe and P.

with IrO_2/C . NiFeP-NW-OER demonstrates obvious improvement in electrocatalytic activity after OER activation. This may be due to the formation of MOOH (NiFe (oxy)hydroxide) during the OER process as well as the presence of P in the structure [6,55]. Moreover, the NiFeP-NW-OER delivers overpotentials of as low as 100 and 129 mV for achieving current densities of 10 and 100 mA cm^{-2} , respectively, which is among the best reported OER electrocatalysts (Table S3, Supporting Information) and is much lower than IrO_2/C (170 and 191 mV) and pure nickel-iron foam after OER activation (151 and 239 mV) (Fig. 3a). The electrochemical performance of the NiFeP-NW and NiFeP-NW-OER electrodes without iR compensation are also shown in Fig. S12a (Supporting Information). The Tafel slope of NiFeP-NW-OER is only 41.1 mV dec^{-1} , which is smaller than NiFe foam-OER (67.4 mV dec^{-1}), NiFeP-NW (55.2 mV dec^{-1}) and IrO_2/C (46.1 mV dec^{-1}), indicating its faster OER kinetics (Fig. 3c). The Faraday efficiency for OER is also tested at 100 mA cm^{-2} . The calculated Faraday efficiency (99.5%) is very close to 100%, which verifies that the anode reaction is completely OER (Fig. S13, Supporting Information). The morphologies of NiFeP samples would significantly affect their OER performance. It can be seen from Fig. S8a–d (Supporting Information) that the morphology of NiFeP changes from nanoparticles to nanowires, nanosheets and thick flakes as the reaction time increases. Among them, the NiFeP nanowires demonstrate the highest OER activity (Fig. S14a, Supporting Information). In addition, the OER activity of the NiFeP catalyst increases when the reaction temperature raises (Fig. S15a, Supporting Information), likely because the amorphous NiFeP prepared at higher temperature demonstrates more uniform nanowire structure (Figs. 1e and S9a, b, Supporting Information). Besides, the added amounts of P during synthesis may also affect the morphologies and OER performance of NiFeP as well as their P contents. The NiFeP sample prepared with the addition of 0.02 mol red phosphorus precursor exhibits the best nanowire morphology with the highest OER activity (Figs. S10a, b and S16a, Supporting Information). Excessive or deficient P precursor would reduce the catalytic activity of NiFeP. The P contents of all NiFeP

samples would decrease after OER test, which may due to its surface reconstruction (Table S1, Supporting Information). Among the NiFeP catalysts, NiFeP-NW-OER with interwoven wire structure and a final P content of 6.63% displays the highest OER activity.

The HER activity of NiFeP-NS and NiFeP-NS-HER is shown in Fig. 3b. Meanwhile, pure nickel-iron foam and Pt/C loaded on nickel-iron foam are selected for comparison. Similar to OER test, the catalytic activity of NiFeP-NS-HER material is significantly improved after HER test. One possible explanation is that the unavoidably formed phosphate on the surface of NiFeP would fall off during HER process, which may expose more active sites. And the phosphorus atom in the nickel-iron foam may optimize the adsorption and desorption of H^* on the active sites, making the material demonstrates excellent HER activity. Linear scan voltammetry of NiFeP-NS-HER shows overpotentials of 83 and 126 mV at HER current densities of 10 and 100 mA cm^{-2} , which is much lower than Pt/C electrodes (90 and 233 mV) and pure nickel-iron foam electrodes (183 and 295 mV) (Fig. 3b), and the HER data without iR compensation is displayed in Fig. S12b (Supporting Information). As shown in Table S4 (Supporting Information), the HER activity of NiFeP-NS-HER can also outperforms most of the reported non-noble metal based HER electrocatalysts. Fig. 3d shows the Tafel slopes of NiFeP-NS ($116.6 \text{ mV dec}^{-1}$), NiFeP-NS-HER (97.0 mV dec^{-1}), pure nickel-iron foam ($107.2 \text{ mV dec}^{-1}$) and Pt/C electrodes ($132.2 \text{ mV dec}^{-1}$). The Tafel slope of NiFeP-NS decreases after HER test, indicating that the HER kinetics of the catalyst materials have been improved after several hours of HER activation. In addition, the Tafel slope of NiFeP-NS-HER falls in the range of $40\text{--}120 \text{ mV dec}^{-1}$, suggesting a possible Volmer-Heyrovsky mechanism. The HER activity of NiFeP with different reaction times, temperatures and the amounts of added red phosphorus are also revealed. And they show similar trends as their OER performance. One different thing is that the NiFeP sample obtained at 9 h with nanosheets morphology demonstrates the highest HER activity as the reaction time increases (Figs. S8e–h and S14b, Supporting Information). The HER activity of the NiFeP catalyst also improves with the increase of the

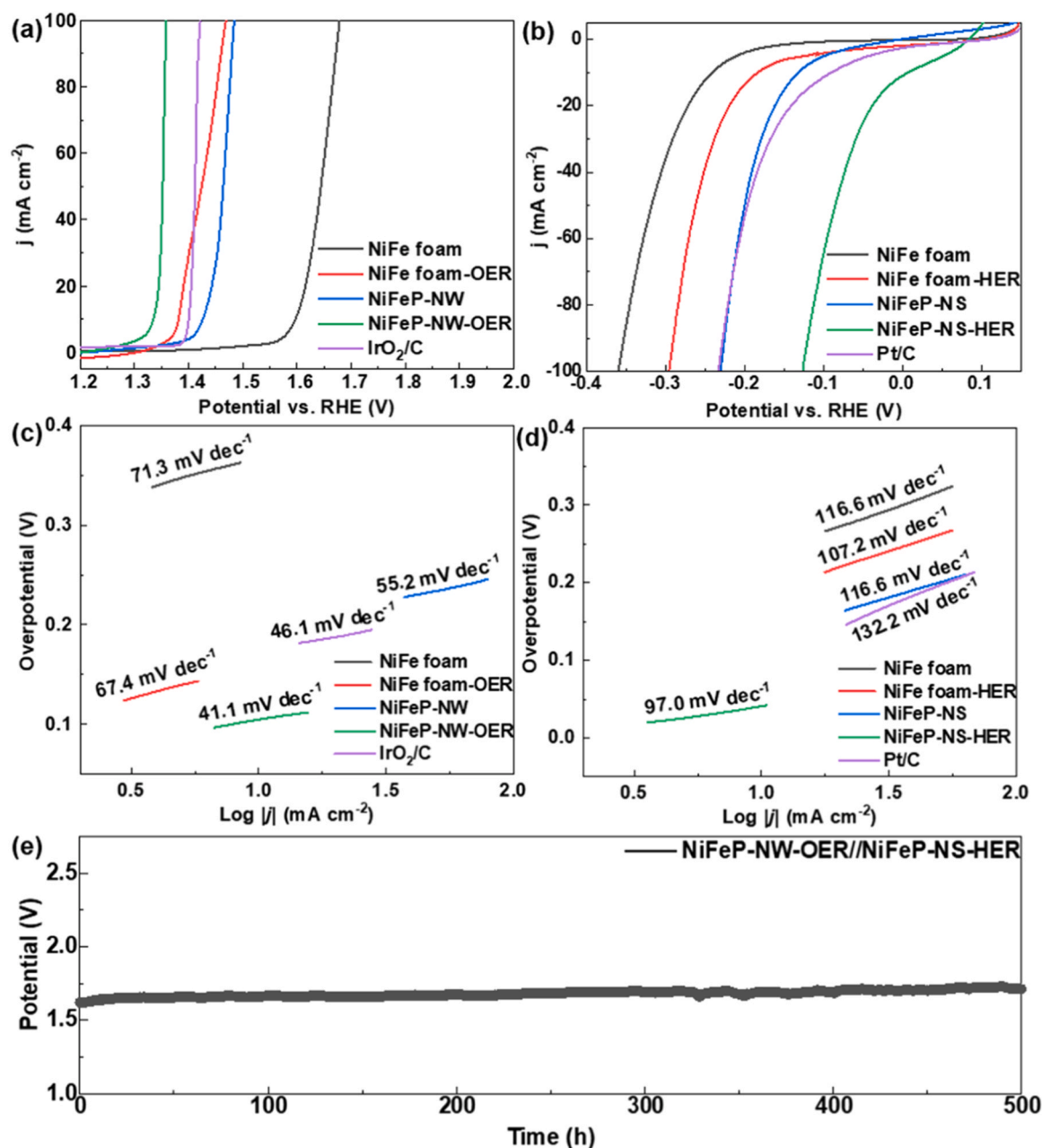


Fig. 3. Electrochemical performance of NiFeP in alkaline simulated seawater (adding 1.0 M KOH and 0.01 M KHCO₃ to 1 M NaCl electrolyte). (a) OER activity of NiFe foam, NiFe foam-OER, NiFeP-NW, NiFeP-NW-OER and IrO₂/C. (b) HER activity of NiFe foam, NiFe foam-HER, NiFeP-NS, NiFeP-NS-HER and Pt/C. (c) Corresponding OER Tafel slopes of NiFe foam, NiFe foam-OER, NiFeP-NW, NiFeP-NW-OER and IrO₂/C. (d) Corresponding HER Tafel slopes of NiFe foam, NiFe foam-HER, NiFeP-NS, NiFeP-NS-HER and Pt/C. (e) Durability tests of NiFeP-NW-OER//NiFeP-NS-HER electrodes under a constant current density of 100 mA cm⁻² for 500 h, with iR compensation.

reaction temperature (Fig. S15b, Supporting Information) as NiFeP-NS-HER displays the best nanosheets morphology (Fig. 1c, f and Fig. S9c, d, Supporting Information). Besides, the NiFeP sample obtained with the addition of 0.02 mol red phosphorus precursor also demonstrates the highest HER activity with abundant nanosheet-like structures (Fig. S16b, Supporting Information). Excessive and deficient P precursor would lead to the formation of larger particles and smaller pieces, respectively (Fig. S10c, d, Supporting Information). Therefore, the surface morphologies as well as P contents of NiFeP samples (Table S2, Supporting Information) can affect the catalytic activity of HER. Among them, NiFeP-NS-HER with nanosheet morphology and a final P content of 10.77% exhibits the highest HER activity. Its HER activity is even higher than the NiFeP-TF-HER with crystalline Ni₁₂P₅ phase, implying

the beneficial of amorphous phosphides structure in HER electrocatalysis.

Due to the excellent OER performance of NiFeP-NW-OER and high HER activity of NiFeP-NS-HER, a two electrode overall alkaline seawater splitting device is assembled (represented as NiFeP-NW-OER//NiFeP-NS-HER). As shown in Fig. 3e, the NiFeP-NW-OER//NiFeP-NS-HER two electrode electrolyzer affords a current density of 100 mA cm⁻² at a low voltage of 1.57 V. After 500 h operation, it still keeps stable with only slight voltage increasement. It can even work at high current density of 1000 mA cm⁻² with a low voltage of 1.80 V after iR compensation (Fig. S17, Supporting Information). The SEM images and polarization curves of NiFeP-NW-OER and NiFeP-NS-HER after 500 h stability test are also carried out. As shown in Fig. S18 (Supporting

Information), after stability test, NiFeP-NW-OER sample undergoes partly surface reconstruction, which may be due to the formation of NiFeOOH, but some nanowires can still be observed. On the other hand, NiFeP-NS-HER basically maintains the nanosheet structure, indicating its better stability. This deduction is certified by the polarization curves of NiFeP materials after 500 h stability test Fig. S19 (Supporting Information). After stability test, the overpotential of NiFeP-NW-OER (500 h) and NiFeP-NS-HER (500 h) materials only increase 65 mV for OER and 25 mV for HER at a current density of 100 mA cm^{-2} , basically maintain the excellent catalytic activity of NiFeP materials. Compared with NiFeP-NW-OER, NiFeP-NS-HER displays a weaker performance decay. The slight degradation of OER and HER catalytic performance may be caused by the surface reconstruction and agglomeration during long-term test. The OER and HER activity of NiFeP-NW-OER and NiFeP-NS-HER in real seawater at alkaline condition are demonstrated in Fig. S20 (Supporting Information). The as-prepared NiFeP-NW-OER catalysts achieve overpotentials of 83 and 147 mV for OER at 10 and 100 mA cm^{-2} and the NiFeP-NS-HER materials display overpotentials of 59 and 130 mV for HER at 10 and 100 mA cm^{-2} respectively in real seawater at alkaline condition. What is more, the NiFeP materials can be operated at a low voltage of 1.62 V with a current density of 100 mA cm^{-2} in real seawater at alkaline condition and demonstrate stable response for more than 100 h, indicating that the as-prepared NiFeP-NW-OER and NiFeP-NS-HER catalysts have high catalytic activity for water splitting even in alkaline real seawater. In order to further study the catalytic activity of NiFeP materials in direct seawater splitting, the OER and HER activity of NiFeP-NW-OER and NiFeP-NS-HER in neutral simulated seawater (1.0 M NaCl, 0.01 M KHCO_3) are tested. The overpotentials of NiFeP-NW-OER and NiFeP-NS-HER at a current density of 100 mA cm^{-2} are 513 mV and 537 mV for OER and HER, respectively (Fig. S21, Supporting Information). Furthermore, the OER and HER activity of NiFeP-NW-OER and NiFeP-NS-HER in neutral real seawater were tested. As shown in Fig. S22 (Supporting Information), the overpotentials of NiFeP-NW-OER and NiFeP-NS-HER at a current density of 100 mA cm^{-2} are 550 mV and 570 mV for OER and HER,

respectively, which confirms the catalytic activity of NiFeP samples for direct seawater splitting. In addition, the electrochemical performance of NiFeP-NW-OER and NiFeP-NS-HER in neutral simulated seawater and neutral real seawater without iR compensation are also shown in Figs. S21 and S22 (Supporting Information).

3.3. Mechanism study

In order to reveal the reason for the enhanced electrocatalytic activity of NiFeP after electrochemical activation, X-ray photoelectron spectroscopy (XPS) was used to study the elemental composition and bonding configuration of NiFeP samples before and after 24 h electrochemical activation. Fig. S23 (Supporting Information) displays the survey spectra of NiFeP-NW and NiFeP-NS before and after electrochemical treatments and certifies the existence of Ni, Fe, P, O. Fig. 4a, b show the high-resolution Fe 2p spectra of NiFeP-NW, NiFeP-NW-OER, NiFeP-NS and NiFeP-NS-HER. The binding energy of $\text{Fe}^{(III)}$ $2p_{3/2}$ peak for NiFeP-NW-OER shifts positively to 713.2 eV compared with the original NiFeP-NW $\text{Fe}^{(III)}$ $2p_{3/2}$ peak (711.9 eV), while the $\text{Fe}^{(III)}$ peak of the NiFeP-NS does not change significantly after HER treatment, suggesting the possible conversion of surface Fe on NiFeP-NW to FeOOH after OER activation [57–59]. The P 2p spectra of NiFeP-NW, NiFeP-NW-OER, NiFeP-NS and NiFeP-NS-HER are shown in Fig. 4c, d. The binding energies of $\text{P}^{(V)}$ $2p_{3/2}$ for NiFeP-NW-OER and NiFeP-NS-HER both shift negatively from 133.5 eV to 132.9 eV after OER or HER activation. The negative shift of the binding energy suggests that the trace phosphate layer that inevitably presents on the phosphide surface during sample preparation [24] is partially consumed after several hours of electrochemical tests. Thus, the phosphate contents on the surface of the catalysts are reduced, which are coordinated with the XRF results (Tables S1 and S2, Supporting Information). Therefore, the internal active sites may be exposed due to the shedding of the phosphate surface layer, and the conductivity of NiFeP catalysts may also be improved. Fig. S24 (Supporting Information) exhibits the Ni 2p spectra of NiFeP-NW and NiFeP-NS. The main Ni $2p_{3/2}$ peak should be ascribed

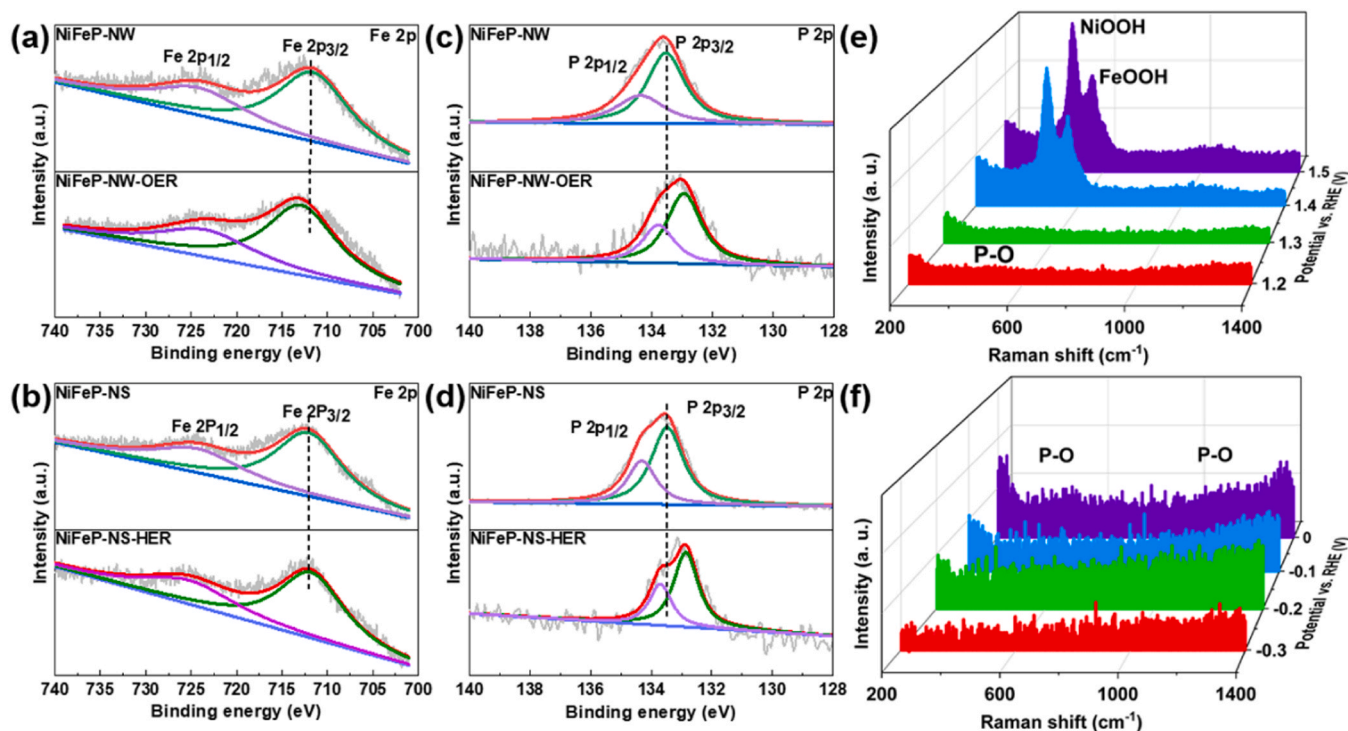


Fig. 4. Spectroscopic characterizations of NiFeP. (a, b) XPS spectra of Fe 2p for NiFeP-NW and NiFeP-NS. (c, d) XPS spectra of P 2p for NiFeP-NW and NiFeP-NS. (e) *In-situ* Raman spectra of NiFeP-NW under the applied potential range from 1.2 V to 1.5 V in alkaline simulated seawater. (f) *In-situ* Raman spectra of NiFeP-NS under the applied potential range from 0 V to -0.3 V in alkaline simulated seawater.

to $\text{Ni}^{\text{II}}/\text{Ni}^{\text{III}}$. The weak peaks at 852.4 eV for NiFeP-NW and NiFeP-NS in Fig. S24a and c (Supporting Information) can be assigned to $\text{Ni}^{(0)}$ on the Ni-Fe foam [60]. After OER activation, the peaks of $\text{Ni}^{(0)}$ in NiFeP-NW disappear, which indicates that the trace nickel metal on the surface of NiFeP-NW is converted to $\text{Ni}^{\text{II}}/\text{Ni}^{\text{III}}$ [61,62]. In addition, after electrochemical activation, the binding energy of $\text{Ni}^{\text{II}}/\text{Ni}^{\text{III}}$

decreases from 857.1 eV to 855.8 eV (NiFeP-NW-OER) and 855.5 eV (NiFeP-NS-HER), respectively, which may correspond to the consumption of surface phosphate. At the same time, the $\text{Ni}^{\text{II}}/\text{Ni}^{\text{III}}$ binding energy of NiFeP-NW-OER is higher than that of NiFeP-NS-HER, which indicates that NiOOH may be formed on the surface of the material after OER.

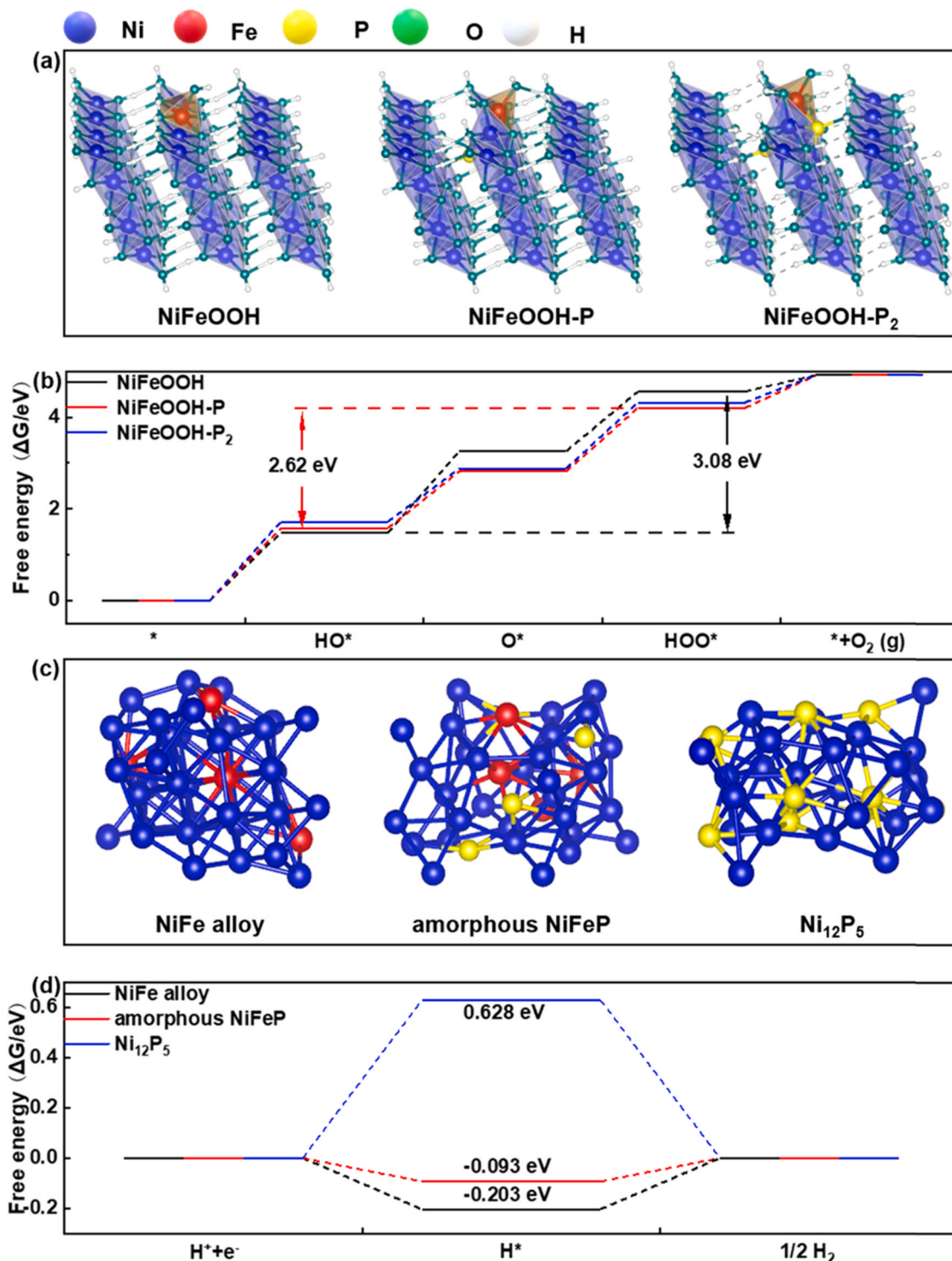


Fig. 5. DFT calculation models and results of OER and HER processes and the Ni, Fe, P, O, H are colored by blue, red, yellow, green and white, respectively. (a) OER calculation models of NiFeOOH without phosphorus atom doping (NiFeOOH), NiFeOOH doped with 1 phosphorus atom (NiFeOOH-P) and 2 phosphorus atoms (NiFeOOH-P₂). (b) OER calculation results of NiFeOOH, NiFeOOH-P and NiFeOOH-P₂. (c) HER calculation models of NiFe alloy without phosphorus atom doping (NiFe alloy), amorphous NiFe doped with phosphorus atoms (amorphous NiFeP) and crystalline Ni₁₂P₅. (d) HER calculation results of NiFe alloy, amorphous NiFeP and Ni₁₂P₅.

To get further insights into the surface structural evolution of NiFeP materials during the electrochemical activation, the NiFeP-NW and NiFeP-NS samples were characterized by in-situ Raman spectroscopy (Fig. 4e, f). The initial Raman spectra of NiFeP-NW at 1.2 V and NiFeP-NS at 0 V both exhibit two weak peaks at 490 cm^{-1} and 1095 cm^{-1} , which can be assigned to the P—O bonds of the surface phosphate [63–65]. For NiFeP-NW, two new peaks appear at 473 cm^{-1} and 551 cm^{-1} when the potential increases to 1.4 V, corresponding to the formation of NiOOH and FeOOH [66], suggesting that the formation of OER active MOOH species could be very quickly during OER test. On the other hand, the peak for P—O bonds on the surface of the NiFeP-NS are greatly reduced after HER treatment. When the potential decreases to -0.3 V , the P—O bonds on the surface of NiFeP-NS almost completely disappear, indicating the decomposition of surface phosphate during HER process [66]. These phenomena are consistent with the XPS and SEM results of NiFeP. The in-situ formed P-containing NiFeOOH on the surface of NiFeP-NW should contribute to its enhanced OER activity, while the degradation of surface phosphate during HER should account for the enhanced HER activity of NiFeP-NS after HER activation.

DFT calculations are used to further illustrate the origin of the high OER and HER activity for amorphous NiFeP and its derivatives. According to XPS and in-situ Raman spectroscopy, a large amount of NiOOH and FeOOH appear on the surface of the electrode during OER while P still remains in the structure. Previous work suggests that Fe is considered to be the OER active site in the NiFe (oxy)hydroxide structure [46]. Therefore, the Fe-on-top structure has been designed and phosphorus atoms with different numbers are incorporated into the neighbors of Ni and Fe to judge the influence of phosphorus atom on the OER kinetics of surface NiFeOOH (Fig. 5a). The reaction mechanism and adsorption structure of all intermediates are shown in Figs. S25–S27 (Supporting Information). According to previous theoretical study, the difference between the adsorption energies of HO^* and HOO^* in the OER path for the oxide catalyst is almost constant ($3.2 \pm 0.2\text{ eV}$), which indicates a universal scaling relation between the adsorption energies of HO^* and HOO^* and causes the high theoretical OER overpotential [14, 67]. In Fig. 5b, the potential gap between the adsorption energies of HO^* and HOO^* for NiFeOOH is calculated to be 3.08 eV . Its rate-determining step is the free energy difference between HO^* and O^* with a barrier of 1.78 eV . Compared with the pure NiFeOOH, the free energy difference between HO^* and HOO^* is significantly reduced for phosphorus atom doped NiFeOOH model. The free energy differences between HO^* and HOO^* for NiFeOOH, NiFeOOH-P (NiFeOOH with 1 phosphorus atom) and NiFeOOH-P₂ (NiFeOOH with 2 phosphorus atoms) are decreased from 3.08 eV to 2.62 eV and 2.60 eV , indicating the theoretical OER overpotential of NiFeOOH may be significantly reduced through the incorporation of a certain number of phosphorus atoms. The ligand effect of incorporated P is suggested to be the main reason for the broken scaling relation of the adsorption energies for HO^* and HOO^* . The rate-determining step of NiFeOOH-P for OER changes from the transformation of HO^* to O^* to the formation of HO^* (1.58 eV). However, when the content of phosphorus atoms is further increased, although the adsorption energy difference between HO^* and HOO^* would still decrease, the adsorption of HO^* on the surface of the catalyst would become more difficult (1.72 eV), resulting in inferior OER activity. Therefore, a new understanding for the designing of highly active OER electrocatalysts by the incorporation of P can be revealed. Moreover, our previous research suggests that the doping of sulfur atom can also reduce the adsorption energy difference between HO^* and HOO^* for NiFeOOH [57], which means that the incorporation of non-metal atoms (such as P, N, S, Se, etc.) may be a general way to break the scaling relations for OER and reduce the high theoretical energy barrier between HO^* and HOO^* , thus optimize the OER kinetics for transition metal oxides.

A nickel-iron alloy structure, an amorphous NiFeP structure, and a crystalline Ni_{12}P_5 structure were also established to explore the HER mechanism of the samples according to the structural characterizations (Fig. 5c). The reaction mechanism and adsorption structure of all

intermediates are shown in Figs. S28–S30 (Supporting Information). As shown in Fig. 5d, the adsorption energy of H^* for nickel-iron alloy, amorphous NiFeP and crystalline Ni_{12}P_5 and calculated to be -0.203 eV , -0.093 eV and 0.628 eV . The amorphous NiFeP demonstrates the smallest absolute value for H^* adsorption energy that is very close to 0 eV , which certifies its enhanced HER activity. Moreover, compared with crystalline Ni_{12}P_5 , the amorphous structure may have higher active site density and unsaturated coordination number due to its long-range disorder and short-range order [68]. Therefore the amorphous NiFeP exhibits the highest HER catalytic activity among the different structures.

4. Conclusion

In summary, we report a facile and environment-friendly method for the fabrication of amorphous NiFeP nanostructures as highly active and stable seawater splitting electrocatalysts. The electronic states of metal sites are suggested to be tuned by the ligand effect of P, thus breaking the scaling relations for adsorbed OER intermediates. Along with the structural engineering and the OER or HER electrochemical treatment, the amorphous NiFeP electrocatalysts exhibit low overpotentials of 100 and 129 mV for OER and 83 and 126 mV for HER at 10 and 100 mA cm^{-2} . The two electrode electrolyzer affords a current density of 100 and 1000 mA cm^{-2} at a low voltage of 1.57 and 1.80 V , respectively, and can operate for over 500 h in alkaline simulate seawater, which is promising for practical applications. XPS and in situ Raman spectra reveal that the surface structure of NiFeP electrodes are reconstructed to NiFeOOH with remained P during OER test and fresh NiFeP surface due to the degradation of surface phosphate during HER test. DFT calculations indicate that the incorporation of phosphorus atoms into NiFeOOH can reduce the adsorption free energy difference between HO^* and HOO^* intermediates from 3.08 eV to 2.62 eV , thus breaks the scaling relations of adsorbed OER intermediates and facilitate the OER kinetics. Consequently, the rate-determining step for OER on oxidized NiFe sites is also changed from the generation of adsorbed O^* to the formation of adsorbed HO^* . On the other hand, the amorphous structure of NiFeP can slightly optimize the adsorption energy of H^* on metal sites compared with crystalline Ni_{12}P_5 and NiFe alloy, resulting in enhanced HER activity. This work proposes a new strategy for the structural engineering of amorphous phosphides as highly efficient alkaline seawater splitting electrocatalysts and may provide universal theoretical guidance for the design of water splitting catalysts.

CRedit authorship contribution statement

Jiayun Liu: Sample preparation, Electrochemical characterization, Data curation, Writing – original draft. **Xuan Liu and Li-ming Yang:** Theoretical calculation. **Hao Shi and Shenzhou Li:** Raman characterization. **Jiahuan Luo and Jiashun Liang:** TEM characterization. **Liang Wang:** SEM characterization. **Tanyuan Wang:** Experimental design. **Tanyuan Wang and Qing Li:** Supervision, Writing – original draft preparation, editing. **Tanyuan Wang, Yunhui Huang and Qing Li:** Mechanism analysis.

Declaration of Competing Interest

The authors declare that they have no known competing financial interests or personal relationships that could have appeared to influence the work reported in this paper.

Acknowledgment

This work was financially supported by National Natural Science Foundation of China (22072051, 21972051, 21801005, 21901008, 22073033, 21873032, 21673087, 21903032), Natural Science Foundation of Guangdong Province (2021A1515012343), the Fundamental

Research Funds for the Central Universities (2019kfyRCPY116) and the Innovation and Talent Recruitment Base of New Energy Chemistry and Device (B21003). The authors thank the Analytical and Testing Center of Huazhong University of Science and Technology (HUST) for carrying out the SEM, XPS, and XRD measurements. The calculations was carried out at the LvLiang Cloud Computing Center of China on TianHe-2 and was supported by the public computing service platform provided by Network and Computing Center of HUST.

Appendix A. Supporting information

Supplementary data associated with this article can be found in the online version at doi:10.1016/j.apcatb.2021.120862.

References

- [1] R. Eisenberg, Rethinking water splitting, *Science* 324 (2009), <https://doi.org/10.1126/science.1172247>, 44-5.
- [2] H. Dotan, A. Landman, S.W. Sheehan, K.D. Malviya, G.E. Shter, D.A. Grave, Z. Arzi, N. Yehudai, M. Halabi, N. Gal, N. Hadari, C. Cohen, A. Rothschild, G.S. Grader, Decoupled hydrogen and oxygen evolution by a two-step electrochemical-chemical cycle for efficient overall water splitting, *Nat. Energy* 4 (2019) 786–795, <https://doi.org/10.1038/s41560-019-0462-7>.
- [3] W. Tong, M. Forster, F. Dionigi, S. Dresp, R. Sadeghi Erami, P. Strasser, A.J. Cowan, P. Farràs, Electrolysis of low-grade and saline surface water, *Nat. Energy* 5 (2020) 367–377, <https://doi.org/10.1038/s41560-020-0550-8>.
- [4] B. Wang, C. Tang, H.-F. Wang, X. Chen, R. Cao, Q. Zhang, A nanosized CoNi hydroxide@hydroxysulfide core-shell heterostructure for enhanced oxygen evolution, *Adv. Mater.* 31 (2019), 1805658, <https://doi.org/10.1002/adma.201805658>.
- [5] X. Tian, P. Zhao, W. Sheng, Hydrogen evolution and oxidation: mechanistic studies and material advances, *Adv. Mater.* 31 (2019), 1808066, <https://doi.org/10.1002/adma.201808066>.
- [6] Z. Pu, J. Zhao, I.S. Amiin, W. Li, M. Wang, D. He, S. Mu, A universal synthesis strategy for P-rich noble metal diphosphide-based electrocatalysts for the hydrogen evolution reaction, *Energy Environ. Sci.* 12 (2019) 952–957, <https://doi.org/10.1039/C9EE00197B>.
- [7] S.Z. Oener, M.J. Foster, S.W. Boettcher, Accelerating water dissociation in bipolar membranes and for electrocatalysis, *Science* 369 (2020) 1099–1103, <https://doi.org/10.1126/science.aaz1487>.
- [8] Q. Wang, C.-Q. Xu, W. Liu, S.-F. Hung, H. Bin Yang, J. Gao, W. Cai, H.M. Chen, J. Li, B. Liu, Coordination engineering of iridium nanocluster bifunctional electrocatalyst for highly efficient and pH-universal overall water splitting, *Nat. Commun.* 11 (2020) 4246, <https://doi.org/10.1038/s41467-020-18064-w>.
- [9] X. Li, L. Liu, X. Ren, J. Gao, Y. Huang, B. Liu, Microenvironment modulation of single-atom catalysts and their roles in electrochemical energy conversion, *Sci. Adv.* 6 (2020) eabb6833, <https://doi.org/10.1126/sciadv.abb6833>.
- [10] Y. Liu, X. Hua, C. Xiao, T. Zhou, P. Huang, Z. Guo, B. Pan, Y. Xie, Heterogeneous spin states in ultrathin nanosheets induce subtle lattice distortion to trigger efficient hydrogen evolution, *J. Am. Chem. Soc.* 138 (2016) 5087–5092, <https://doi.org/10.1021/jacs.6b00858>.
- [11] W. Li, F. Li, H. Yang, X. Wu, P. Zhang, Y. Shan, L. Sun, A bio-inspired coordination polymer as outstanding water oxidation catalyst via second coordination sphere engineering, *Nat. Commun.* 10 (2019) 5074, <https://doi.org/10.1038/s41467-019-13052-1>.
- [12] L. Yu, L. Wu, B. McElhenny, S. Song, D. Luo, F. Zhang, Y. Yu, S. Chen, Z. Ren, Ultrafast room-temperature synthesis of porous S-doped Ni/Fe (oxy)hydroxide electrodes for oxygen evolution catalysis in seawater splitting, *Energy Environ. Sci.* 13 (2020) 3439–3446, <https://doi.org/10.1039/D0EE00921K>.
- [13] Y. Liu, C. Xiao, P. Huang, M. Cheng, Y. Xie, Regulating the charge and spin ordering of two-dimensional ultrathin solids for electrocatalytic water splitting, *Chem* 4 (2018) 1263–1283, <https://doi.org/10.1016/j.chempr.2018.02.006>.
- [14] I.C. Man, H.-Y. Su, F. Calle-Vallejo, H.A. Hansen, J.I. Martínez, N.G. Inoglu, J. Kitchin, T.F. Jaramillo, J.K. Nørskov, J. Rossmeisl, Universality in oxygen evolution electrocatalysis on oxide surfaces, *ChemCatChem* 3 (2011) 1159–1165, <https://doi.org/10.1002/cctc.201000397>.
- [15] R.D.L. Smith, M.S. Prévot, R.D. Fagan, Z. Zhang, P.A. Sedach, M.K.J. Siu, S. Trudel, C.P. Berlinguette, Photochemical route for accessing amorphous metal oxide materials for water oxidation catalysis, *Science* 340 (2013), <https://doi.org/10.1126/science.1233638>, 60-3.
- [16] S. Li, J. Liu, S. Duan, T. Wang, Q. Li, Tuning the oxygen evolution electrocatalysis on NiFe-layered double hydroxides via sulfur doping, *Chin. J. Catal.* 41 (2020) 847–852, [https://doi.org/10.1016/S1872-2067\(19\)63356-5](https://doi.org/10.1016/S1872-2067(19)63356-5).
- [17] J. Liang, Y. Jiao, M. Jaroniec, S.Z. Qiao, Sulfur and nitrogen dual-doped mesoporous graphene electrocatalyst for oxygen reduction with synergistically enhanced performance, *Angew. Chem. Int. Ed.* 51 (2012) 11496–11500, <https://doi.org/10.1002/anie.201206720>.
- [18] Y. Zhou, J.L. Silva, J.M. Woods, J.V. Pondick, Q. Feng, Z. Liang, W. Liu, L. Lin, B. Deng, B. Brena, F. Xia, H. Peng, Z. Liu, H. Wang, C.M. Araujo, J.J. Cha, Revealing the contribution of individual factors to hydrogen evolution reaction catalytic activity, *Adv. Mater.* 30 (2018), 1706076, <https://doi.org/10.1002/adma.201706076>.
- [19] J.-Q. Chi, K.-L. Yan, Z. Xiao, B. Dong, X. Shang, W.-K. Gao, X. Li, Y.-M. Chai, C.-G. Liu, Trimetallic NiFeCo selenides nanoparticles supported on carbon fiber cloth as efficient electrocatalyst for oxygen evolution reaction, *Int. J. Hydrog. Energy* 42 (2017) 20599–20607, <https://doi.org/10.1016/j.ijhydene.2017.06.219>.
- [20] S. Niu, W.-J. Jiang, Z. Wei, T. Tang, J. Ma, J.-S. Hu, L.-J. Wan, Se-doping activates FeOOH for cost-effective and efficient electrochemical water oxidation, *J. Am. Chem. Soc.* 141 (2019) 7005–7013, <https://doi.org/10.1021/jacs.9b01214>.
- [21] N. Han, P. Liu, J. Jiang, L. Ai, Z. Shao, S. Liu, Recent advances in nanostructured metal nitrides for water splitting, *J. Mater. Chem. A* 6 (2018) 19912–19933, <https://doi.org/10.1039/C8TA06529B>.
- [22] Y. Xue, D. Yu, L. Dai, R. Wang, D. Li, A. Roy, F. Lu, H. Chen, Y. Liu, J. Qu, Three-dimensional B,N-doped graphene foam as a metal-free catalyst for oxygen reduction reaction, *Phys. Chem. Chem. Phys.* 15 (2013) 12220–12226, <https://doi.org/10.1039/C3CP51942B>.
- [23] A. Dutta, N. Pradhan, Developments of metal phosphides as efficient OER precatalysts, *J. Phys. Chem. Lett.* 8 (2017) 144–152, <https://doi.org/10.1021/acs.jpclett.6b02249>.
- [24] T. Wang, C. Wang, Y. Jin, A. Sviripa, J. Liang, J. Han, Y. Huang, Q. Li, G. Wu, Amorphous Co–Fe–P nanospheres for efficient water oxidation, *J. Mater. Chem. A* 5 (2017) 25378–25384, <https://doi.org/10.1039/C7TA08720A>.
- [25] A. Grimaud, A. Demortière, M. Saubanière, W. Dachraoui, M. Duchamp, M.-L. Doublet, J.-M. Tarascon, Activation of surface oxygen sites on an iridium-based model catalyst for the oxygen evolution reaction, *Nat. Energy* 2 (2016) 16189, <https://doi.org/10.1038/nenergy.2016.189>.
- [26] R.R. Rao, M.J. Kolb, L. Giordano, A.F. Pedersen, Y. Katayama, J. Hwang, A. Mehta, H. You, J.R. Linger, H. Zhou, N.B. Halck, T. Vegge, I. Chorkendorff, I.E. L. Stephens, Y. Shao-Horn, Operando identification of site-dependent water oxidation activity on ruthenium dioxide single-crystal surfaces, *Nat. Catal.* 3 (2020) 516–525, <https://doi.org/10.1038/s41929-020-0457-6>.
- [27] I.T. McCrum, M.T.M. Koper, The role of adsorbed hydroxide in hydrogen evolution reaction kinetics on modified platinum, *Nat. Energy* 5 (2020) 891–899, <https://doi.org/10.1038/s41560-020-00710-8>.
- [28] S. Chen, J. Duan, Y. Zheng, X. Chen, X.W. Du, M. Jaroniec, S.-Z. Qiao, Ionic liquid-assisted synthesis of N/S-double doped graphene microwires for oxygen evolution and Zn–air batteries, *Energy Storage Mater.* 1 (2015) 17–24, <https://doi.org/10.1016/j.ensm.2015.08.001>.
- [29] Y. Zhou, J.V. Pondick, J.L. Silva, J.M. Woods, D.J. Hynek, G. Matthews, X. Shen, Q. Feng, W. Liu, Z. Lu, Z. Liang, B. Brena, Z. Cai, M. Wu, L. Jiao, S. Hu, H. Wang, C. M. Araujo, J.J. Cha, Unveiling the interfacial effects for enhanced hydrogen evolution reaction on MoS₂/WTe₂ hybrid structures, *Small* 15 (2019), 1900078, <https://doi.org/10.1002/sml.201900078>.
- [30] M. Elimelech, W.A. Phillip, The future of seawater desalination: energy, technology, and the environment, *Science* 333 (2011), <https://doi.org/10.1126/science.1200488>, 712-7.
- [31] Y. Zhao, B. Jin, Y. Zheng, H. Jin, Y. Jiao, S.-Z. Qiao, Charge state manipulation of cobalt selenide catalyst for overall seawater electrolysis, *Adv. Energy Mater.* 8 (2018), 1801926, <https://doi.org/10.1002/aenm.201801926>.
- [32] S. Dresp, F. Dionigi, M. Klingenhof, P. Strasser, Direct electrolytic splitting of seawater: opportunities and challenges, *ACS Energy Lett.* 4 (2019) 933–942, <https://doi.org/10.1021/acsenenergylett.9b00220>.
- [33] S. Zhang, W. Wang, F. Hu, Y. Mi, S. Wang, Y. Liu, X. Ai, J. Fang, H. Li, T. Zhai, 2D CoOH sheet-encapsulated Ni₂P into tubular arrays realizing 1000 mA cm⁻² level-current-density hydrogen evolution Over 100h in neutral water, *Nanomicro Lett.* 12 (2020) 140, <https://doi.org/10.1007/s40820-020-00476-4>.
- [34] L. Yu, Q. Zhu, S. Song, B. McElhenny, D. Wang, C. Wu, Z. Qin, J. Bao, Y. Yu, S. Chen, Z. Ren, Non-noble metal-nitride based electrocatalysts for high-performance alkaline seawater electrolysis, *Nat. Commun.* 10 (2019) 5106, <https://doi.org/10.1038/s41467-019-13092-7>.
- [35] Y. Kuang, M.J. Kenney, Y. Meng, W.-H. Hung, Y. Liu, J.E. Huang, R. Prasanna, P. Li, Y. Li, L. Wang, M.-C. Lin, M.D. McGehee, X. Sun, H. Dai, Solar-driven, highly sustained splitting of seawater into hydrogen and oxygen fuels, *Proc. Natl. Acad. Sci.* 116 (2019) 6624–6629, <https://doi.org/10.1073/pnas.1900556116>.
- [36] H. Jin, X. Liu, A. Vasileff, Y. Jiao, Y. Zhao, Y. Zheng, S.-Z. Qiao, Single-crystal nitrogen-rich two-dimensional MoS₂ nanosheets for efficient and stable seawater splitting, *ACS Nano* 12 (2018) 12761–12769, <https://doi.org/10.1021/acsnano.8b07841>.
- [37] S. Dresp, T. Ngo Thanh, M. Klingenhof, S. Brückner, P. Hauke, P. Strasser, Efficient direct seawater electrolyzers using selective alkaline NiFe-LDH as OER catalyst in asymmetric electrolyte feeds, *Energy Environ. Sci.* 13 (2020) 1725–1729, <https://doi.org/10.1039/D0EE01125H>.
- [38] F. Dionigi, T. Reier, Z. Pawolek, M. Glicke, P. Strasser, Design criteria, operating conditions, and nickel-iron hydroxide catalyst materials for selective seawater electrolysis, *ChemSusChem* 9 (2016) 962–972, <https://doi.org/10.1002/cssc.201501581>.
- [39] Y. Shi, M. Li, Y. Yu, B. Zhang, Recent advances in nanostructured transition metal phosphides: synthesis and energy-related applications, *Energy Environ. Sci.* 13 (2020) 4564–4582, <https://doi.org/10.1039/D0EE02577A>.
- [40] H.B. Li, M.H. Yu, F.X. Wang, P. Liu, Y. Liang, J. Xiao, C.X. Wang, Y.X. Tong, G. W. Yang, Amorphous nickel hydroxide nanospheres with ultrahigh capacitance and energy density as electrochemical pseudocapacitor materials, *Nat. Commun.* 4 (2013) 1894, <https://doi.org/10.1038/ncomms2932>.
- [41] C. Ray, S.C. Lee, K.V. Sankar, B. Jin, J. Lee, J.H. Park, S.C. Jun, Amorphous phosphorus-incorporated cobalt molybdenum sulfide on carbon cloth: an efficient and stable electrocatalyst for enhanced overall water splitting over entire pH

- values, *ACS Appl. Mater. Interfaces* 9 (2017) 37739–37749, <https://doi.org/10.1021/acsami.7b11192>.
- [42] G. Kresse, J. Furthmüller, Efficient iterative schemes for ab initio total-energy calculations using a plane-wave basis set, *Phys. Rev. B* 54 (1996) 11169–11186, <https://doi.org/10.1103/PhysRevB.54.11169>.
- [43] G. Kresse, J. Furthmüller, Efficiency of ab-initio total energy calculations for metals and semiconductors using a plane-wave basis set, *Comput. Mater. Sci.* 6 (1996) 15–50, [https://doi.org/10.1016/0927-0256\(96\)00008-0](https://doi.org/10.1016/0927-0256(96)00008-0).
- [44] J.P. Perdew, M. Ernzerhof, K. Burke, Rationale for mixing exact exchange with density functional approximations, *J. Chem. Phys.* 105 (1996) 9982–9985, <https://doi.org/10.1063/1.472933>.
- [45] S. Grimme, Semiempirical GGA-type density functional constructed with a long-range dispersion correction, *J. Comput. Chem.* 27 (2006) 1787–1799, <https://doi.org/10.1002/jcc.20495>.
- [46] D. Friebe, M.W. Louie, M. Bajdich, K.E. Sanwald, Y. Cai, A.M. Wise, M.-J. Cheng, D. Sokaras, T.-C. Weng, R. Alonso-Mori, R.C. Davis, J.R. Bargar, J.K. Nørskov, A. Nilsson, A.T. Bell, Identification of highly active Fe sites in (Ni,Fe)OOH for electrocatalytic water splitting, *J. Am. Chem. Soc.* 137 (2015) 1305–1313, <https://doi.org/10.1021/ja511559d>.
- [47] L. Yang, Z. Guo, J. Huang, Y. Xi, R. Gao, G. Su, W. Wang, L. Cao, B. Dong, Vertical growth of 2D amorphous FePO₄ nanosheet on Ni foam: outer and inner structural design for superior water splitting, *Adv. Mater.* 29 (2017), 1704574, <https://doi.org/10.1002/adma.201704574>.
- [48] J. Hu, W. Chen, X. Zhao, X. Cao, J. Zhu, Z. Chen, Stable active sites on Ni₁₂P₅ surfaces for the hydrogen evolution reaction, *Energy Technol.* 7 (2019), 1900013, <https://doi.org/10.1002/ente.201900013>.
- [49] J.K. Nørskov, J. Rossmeisl, A. Logadottir, L. Lindqvist, J.R. Kitchin, T. Bligaard, H. Jónsson, Origin of the overpotential for oxygen reduction at a fuel-cell cathode, *J. Phys. Chem. B* 108 (2004) 17886–17892, <https://doi.org/10.1021/jp047349j>.
- [50] J.K. Nørskov, T. Bligaard, A. Logadottir, J.R. Kitchin, J.G. Chen, S. Pandalov, U. Stimming, Trends in the exchange current for hydrogen evolution, *J. Electrochem. Soc.* 152 (2005) J23, <https://doi.org/10.1149/1.1856988>.
- [51] J.H. Zhan, X.G. Yang, D.W. Wang, S.D. Li, Y. Xie, Y. Xia, Y. Qian, Polymer-controlled growth of CdS nanowires, *Adv. Mater.* 12 (2000) 1348–1351, [https://doi.org/10.1002/1521-4095\(200009\)12:18<1348::AID-ADMA1348>3.0.CO;2-X](https://doi.org/10.1002/1521-4095(200009)12:18<1348::AID-ADMA1348>3.0.CO;2-X).
- [52] J. Ma, Y. Wang, Y. Wang, P. Peng, J. Lian, X. Duan, Z. Liu, X. Liu, Q. Chen, T. Kim, G. Yao, W. Zheng, One-dimensional Sb₂Se₃ nanostructures: solvothermal synthesis, growth mechanism, optical and electrochemical properties, *CrystEngComm* 13 (2011) 2369–2374, <https://doi.org/10.1039/C0CE000381F>.
- [53] Y.-D. Li, H.-W. Liao, Y. Ding, Y.-T. Qian, L. Yang, G.-E. Zhou, Nonaqueous synthesis of CdS nanorod semiconductor, *Chem. Mater.* 10 (1998) 2301–2303, <https://doi.org/10.1021/cm970789l>.
- [54] M. Ledendecker, S. Krick Calderón, C. Papp, H.-P. Steinrück, M. Antonietti, M. Shalom, The synthesis of nanostructured Ni₅P₄ films and their use as a non-noble bifunctional electrocatalyst for full water splitting, *Angew. Chem. Int. Ed.* 54 (2015) 12361–12365, <https://doi.org/10.1002/anie.201502438>.
- [55] H. Liu, L. Yang, K. Qiao, X. Zeng, Y. Huang, L. Zheng, D. Cao, A new concept analogous to homogeneous catalysis to construct in-situ regenerative electrodes for long-term oxygen evolution reaction, *Nano Energy* 76 (2020), 105115, <https://doi.org/10.1016/j.nanoen.2020.105115>.
- [56] L. Ji, J. Wang, X. Teng, T.J. Meyer, Z. Chen, CoP nanoframes as bifunctional electrocatalysts for efficient overall water splitting, *ACS Catal.* 10 (2020) 412–419, <https://doi.org/10.1021/acscatal.9b03623>.
- [57] T. Wang, G. Nam, Y. Jin, X. Wang, P. Ren, M.G. Kim, J. Liang, X. Wen, H. Jang, J. Han, Y. Huang, Q. Li, J. Cho, NiFe (oxy) hydroxides derived from nife disulfides as an efficient oxygen evolution catalyst for rechargeable Zn–air batteries: the effect of surface S residues, *Adv. Mater.* 30 (2018), 1800757, <https://doi.org/10.1002/adma.201800757>.
- [58] J. Chen, F. Zheng, S.-J. Zhang, A. Fisher, Y. Zhou, Z. Wang, Y. Li, B.-B. Xu, J.-T. Li, S.-G. Sun, Interfacial interaction between FeOOH and Ni–Fe LDH to modulate the local electronic structure for enhanced OER electrocatalysis, *ACS Catal.* 8 (2018) 11342–11351, <https://doi.org/10.1021/acscatal.8b03489>.
- [59] W.D. Chemelewski, H.-C. Lee, J.-F. Lin, A.J. Bard, C.B. Mullins, Amorphous FeOOH oxygen evolution reaction catalyst for photoelectrochemical water splitting, *J. Am. Chem. Soc.* 136 (2014) 2843–2850, <https://doi.org/10.1021/ja411835a>.
- [60] P. Prieto, V. Nistor, K. Nouneh, M. Oyama, M. Abd-Lefdil, R. Díaz, XPS study of silver, nickel and bimetallic silver–nickel nanoparticles prepared by seed-mediated growth, *Appl. Surf. Sci.* 258 (2012) 8807–8813, <https://doi.org/10.1016/j.apsusc.2012.05.095>.
- [61] T. Wang, M. Wang, H. Yang, M. Xu, C. Zuo, K. Feng, M. Xie, J. Deng, J. Zhong, W. Zhou, T. Cheng, Y. Li, Weakening hydrogen adsorption on nickel via interstitial nitrogen doping promotes bifunctional hydrogen electrocatalysis in alkaline solution, *Energy Environ. Sci.* 12 (2019) 3522–3529, <https://doi.org/10.1039/C9EE01743G>.
- [62] H. Huang, C. Yu, C. Zhao, X. Han, J. Yang, Z. Liu, S. Li, M. Zhang, J. Qiu, Iron-tuned super nickel phosphide microstructures with high activity for electrochemical overall water splitting, *Nano Energy* 34 (2017) 472–480, <https://doi.org/10.1016/j.nanoen.2017.03.016>.
- [63] Y. Zeng, S. Zhou, In situ surface Raman study of the phosphorus incorporation mechanism during electrodeposition of Ni–P alloys, *J. Electroanal. Chem.* 469 (1999) 79–83, [https://doi.org/10.1016/S0022-0728\(99\)00179-5](https://doi.org/10.1016/S0022-0728(99)00179-5).
- [64] L. Zhang, R.K. Brow, A. Raman, Study of iron–phosphate crystalline compounds and glasses, *J. Am. Ceram. Soc.* 94 (2011) 3123–3130, <https://doi.org/10.1111/j.1551-2916.2011.04486.x>.
- [65] P. Stoch, A. Stoch, M. Ciecinska, I. Krakowiak, M. Sitarz, Structure of phosphate and iron-phosphate glasses by DFT calculations and FTIR/Raman spectroscopy, *J. Non Cryst. Solids* 450 (2016) 48–60, <https://doi.org/10.1016/j.jnoncrysol.2016.07.027>.
- [66] S. Duan, Z. Liu, H. Zhuo, T. Wang, J. Liu, L. Wang, J. Liang, J. Han, Y. Huang, Q. Li, Hydrochloric acid corrosion induced bifunctional free-standing NiFe hydroxide nanosheets towards high-performance alkaline seawater splitting, *Nanoscale* 12 (2020) 21743–21749, <https://doi.org/10.1039/D0NR05458E>.
- [67] R. Christensen, H.A. Hansen, C.F. Dickens, J.K. Nørskov, T. Vegge, Functional independent scaling relation for ORR/OER catalysts, *J. Phys. Chem. C* 120 (2016) 24910–24916, <https://doi.org/10.1021/acs.jpcc.6b09141>.
- [68] W. Xu, H. Wang, Earth-abundant amorphous catalysts for electrolysis of water, *Chin. J. Catal.* 38 (2017) 991–1005, [https://doi.org/10.1016/S1872-2067\(17\)62810-9](https://doi.org/10.1016/S1872-2067(17)62810-9).